Chapter 5

Polyaniline Nanotube/Reduced Graphene Oxide Aerogel as Efficient Counter Electrode for Quasi-Solid-State Dye Sensitized Solar Cells

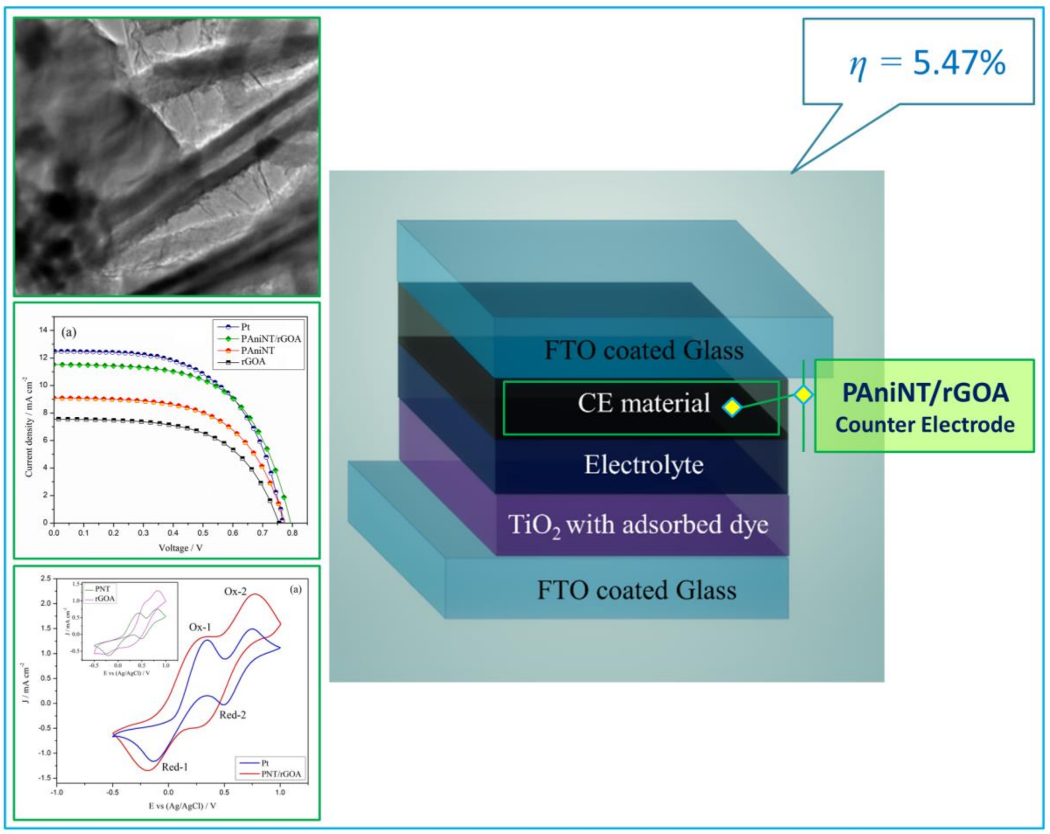

DSSC fabricated with PAniNT/rGOA as the counter electrode exhibits an efficiency of 5.47%, wherein rGOA provides a high surface area support for PAniNTs, which acts as an electro-catalyst for triiodide reduction.

5.1 Introduction

With the aim to combine the electro-catalytic property of polyaniline nanotube (PAniNT) and electro-conductivity of graphene aerogel, in the present study PAniNT/reduced graphene oxide aerogel (PAniNT/rGOA) is synthesized and studied as a counter electrode material for dye sensitized solar cell (DSSC).

Conducting polymers such as polyaniline (PAni), poly(3,4‒ethylenedioxythiophene) (PEDOT) and polypyrrole have great potential to be used as alternatives for the Pt counter electrode [1–7]. PAni is considered as one of the most preferred alternatives amongst them because of its low cost, high electrochemical activity and environmental stability. On the other hand, earth abundant carbonaceous materials also present a great potential to replace platinum (Pt) because of their high electric conductivities and better chemical resistance to iodine. In the recent years, a wide range of carbonaceous materials like carbon nanotubes, graphene, carbon black, activated carbon and carbon-based composites have drawn research attention as Pt free counter electrodes [8–14]. In particular, graphene aerogels have a great prospect to become an efficient counter electrode material because of its unique qualities [15]. Graphene aerogels are three-dimensionally interconnected graphene sheets having a mesoporous structure. They exhibit much faster charge transport across the graphene sheets in comparison to the porous structures constructed by physically and randomly staked graphene sheets because of the much higher electrical conductivities [16]. Furthermore, their large pore volume facilitates the mass transfer of redox species.

Xue et al. (2012) for the first time prepared a nitrogen-doped 3D graphene foam and demonstrated its application as a metal-free electro-catalyst for the reduction of triiodide to replace the Pt cathode in DSSCs, leading to a efficiency value of upto 7.07% [17]. Yang et al. (2014) prepared a flexible counter electrode based on nitrogen-doped carbon aerogels exhibiting efficiency of 8.83% [18]. The aerogel was prepared by introducing tripolycyanamide during synthesis of the organic aerogel precursors. Carbon based aerogel with high surface area is a promising alternative to the expensive Pt counter electrode.

This part of the thesis has been communicated with:

Mohan, K., Bora, A., Roy, R. S., Nath, B. C., and Dolui, S. K. Polyaniline nanotube / reduced graphene oxide aerogel as efficient counter electrode for quasi solid state dye sensitized solar cell. *Journal of Power Sources. (Revised).*

5.2 Experimental

5.2.1 Materials

Graphite flakes, sulfuric acid (H_2SO_4), sodium nitrate ($NaNO_3$), potassium permanganate ($KMnO_4$), hydrogen peroxide (H_2O_2), hydrochloric acid (HCl), resorcinol, formaldehyde, Sodium carbonate (Na_2CO_3), aniline, ammonium persulfate (APS), acetic acid and methanol were purchased from Aldrich. All other materials used for the device fabrication were same as mentioned in Section 2.2.1 of Chapter 2.

5.2.2. Preparation of graphene oxide

The precursor material, graphene oxide (GO), used for the preparation of the aerogels was prepared using modified Hummers method [19]. For typical synthesis of GO, 23 mL concentrated H_2SO_4 was added with 1g graphite flakes and 0.5 g $NaNO_3$. This reaction mixture was stirred for 4 h in an ice bath. 3 mL $KMnO_4$ was added slowly into the solution keeping the temperature below 15°C, followed by slow addition of 184 mL water with continuous stirring for another 2 h. The reaction mixture was then transferred to a warm water bath maintained at 35°C for 2 h under stirring. It was then refluxed at 98°C for 10-15 min followed by lowering the temperature to 25-30°C, at which the solution turned brown. 8 mL H_2O_2 was added after stirring for another 2 hours at that temperature whereupon the color of the solution changed from brown to yellow. The product was finally filtered and washed with 10% HCl solution and deionized water, and dried in vacuum oven.

5.2.3 Preparation of reduced graphene oxide aerogel

In the preparation of reduced graphene oxide aerogel (rGOA), 0.4 g GO was mixed in 40 mL deionized water in a 100 mL beaker and sonicated for 10 min to get (10 mg mL^{-1}) GO suspension. Subsequently, 0.674 g resorcinol, 0.724 g formaldehyde and 3.23 mg Na_2CO_3 were added to the GO suspension and stirred for 30 min. The prepared suspension was sealed in a beaker and transferred to an oven maintained at 85°C for 3 days. Afterward, the rGO hydrogel obtained was washed with water, and freeze-dried for 24 h to completely remove the water and obtain rGO aerogel [15].

5.2.4 Preparation of polyaniline nanotube/reduced graphene oxide aerogel

PAniNT was prepared by using aniline monomer and APS solutions [20]. The two separate solutions were prepared in an aqueous solution of 0.4 M acetic acid and 1 M methanol in water and were kept in 0-5°C for 30 min. Both the solutions were then mixed and stirred vigorously for 30 s followed by keeping the mixture undisturbed overnight at 0-5°C to get maximum precipitation. Finally, the precipitate was washed with deionized water and dried to obtain PAniNT. The as-prepared PAniNT and GO were used to make the aerogel. In two separate 50 mL beakers, 0.2 g of GO and PAniNT were sonicated in 20 mL of deionized water to get 10 mg mL^{-1} GO and PAniNT suspensions. Then in the GO suspension, 0.337 g resorcinol, 0.362 g formaldehyde and 1.6 mg Na_2CO_3 were added and stirred for 30 min. The two suspensions were then mixed in a 100 mL beaker and sealed. The sealed beaker with the suspension was kept in an oven maintained at 85°C for 3 days to get the PAniNT/rGO hydrogel. Finally, the aerogel with mass ratio 1:1 (PAniNT/rGOA) was obtained by washing the hydrogel with deionized water followed by freeze-drying for 24 hours. Aerogels with different amount of PAniNT (6, 8 and 12 mg mL^{-1}) with GO (10 mg ml^{-1}) suspension were also prepared for comparison purposes. The prepared aerogels were named as PAniNT/rGOA(0.6), PAniNT/rGOA(0.8), PAniNT/rGOA and PAniN/rGOA(1.2) with 6, 8, 10 and 12 mg mL^{-1} of PAniNTs with 10 mg mL^{-1} in GO respectively.

5.2.5 DSSC fabrication

The polymer gel electrolyte (PGE) was prepared by dispersing poly(methyl methacrylate) (PMMA) with 0.57 wt% of carbon black (CB) in liquid electrolyte according to the protocol previously reported in Section 3.2.2 of Chapter 3 [21]. N719 dye sensitized titanium dioxide (TiO_2) photoanode was fabricated by following the procedure described in Section 2.2.5 of Chapter 2.

For preparing the counter electrodes, aerogel pastes were prepared by dispersing 10 mg of the aerogels in 0.5 mL 0.5% Nafion solution by sonicating for 10 min. Using doctor blade method, the prepared aerogel pastes were cast onto a cleaned fluorine doped tin oxide (FTO) glass to make the counter electrode, followed by heating at 80°C. For comparison purpose, Pt counter electrode was also prepared by following spin coating and chemical reduction methods as described in Section 2.2.5 of Chapter 2.

Finally, the DSSCs were assembled by sandwiching the PGE between the photoanode and the counter electrode using 25 μm thick Solaronix thermal polymer spacers. The internal spacer gap between the two electrodes was completely filled by the electrolyte, following which the devices were kept at 60°C for 5 min to improve the interfacial contact between the electrolyte and the electrodes [22,23].

5.2.6 Characterization

For structural characterization of the aerogels, the Fourier transform infrared (FTIR) spectra of the prepared samples were recorded. The Raman spectra and the X-ray diffraction (XRD) patterns of the samples were recorded on a Renishaw basis series with 514 lasers and Bruker AXS instrument respectively. Scanning electron microscope (SEM) and transmission electron microscope (TEM) micrographs were obtained to study the surface morphology. Nitrogen adsorption/desorption isotherms were obtained by a Quantachrome NOVA 1000E Brunauer-Emmett-Teller (BET) apparatus. Bio-Logic SP-150 potentiostat was used to record the cyclic voltammogram of the fabricated device in the potential range of -0.5 V to 1.0 V under 1 sun illumination. Current density-voltage (J-V) characteristics data were used to calculate the fill factors (FF) and photoconversion efficiencies (η) of DSSCs [24]. The same electrochemical workstation was also used to explore the electrochemical impedance spectroscopy (EIS), Tafel data and the chemical capacitance ($C\mu$) at both the electrode/electrolyte interfaces.

5.3 Results and discussion

5.3.1 Structural analyses

5.3.1.1 FTIR spectroscopy analysis

The FTIR spectra of the prepared PAniNT, GO, rGOA and PAniNT/rGOA are shown in **Figure 5.1**. In the characteristic spectrum of PAniNT, the peaks at 3421 cm^{-1}, 1558 cm^{-1} and 1472 cm^{-1} appear due to N-H stretching, and C=C stretching of the quinoid and the benzoid ring respectively [25]. The peaks at 1304 cm^{-1}, 1249 cm^{-1}, 1113 cm^{-1} and 812 cm^{-1} appear due C-N stretching, C–N–C stretching, N-Q-N vibration and asymmetric 1, 4-disubstituted benzoid ring vibrations respectively. In the characteristic peaks of GO, the oxidation of graphite to GO is established by the appearance of peaks at 1736 cm^{-1}, 1640 cm^{-1} and 1055 cm^{-1}, typical of presence of carbonyl moiety, C=O vibrations in carboxylic acid and alkoxy C-O stretching vibrations respectively [26]. The peaks at 3440 cm^{-1} and 1402 cm^{-1} are assigned to O-H stretching and deformation vibration mode of intercalated water in the GO. In the spectra of rGOA, some of the peaks disappear while the intensities of peaks at 3440 cm^{-1}, 1736 cm^{-1} and 1402 cm^{-1} decrease, signifying the elimination of oxygen containing groups in rGOA to a high extent during aerogel formation. PAniNT/rGOA exhibits typical absorption peaks of both the constituting components suggesting that the desired composite aerogel is formed successfully. Partial reduction of GO to reduced graphene oxide (rGO) during the synthesis procedure is indicated by the disappearance of peaks of oxygen containing groups. Additionally, the intensities of the peaks at 3440 cm^{-1}, 1736 cm^{-1} and 1402 cm^{-1} also decrease in the spectra of PAniNT/rGOA.

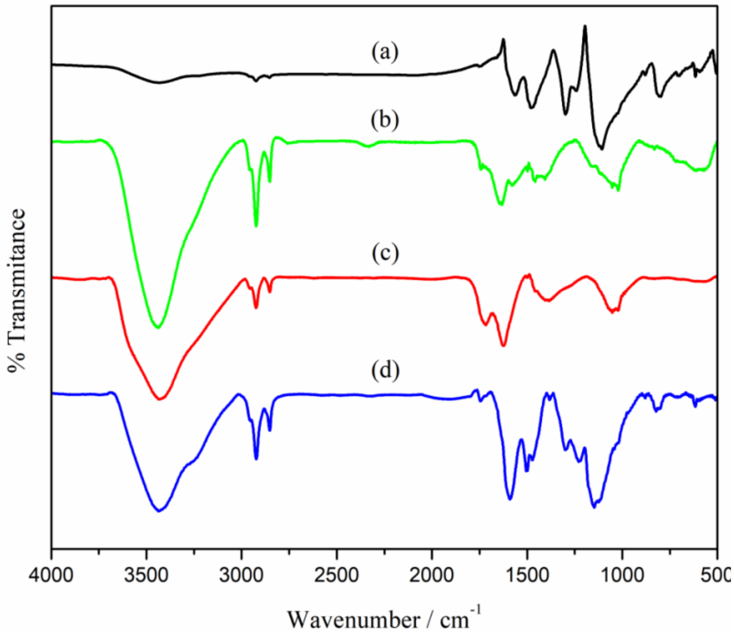

Figure 5.1. FTIR spectra of **(a)** PAniNT, **(b)** GO, **(c)** rGOA and **(d)** PAniNT/rGOA.

5.3.1.2 Raman spectroscopy analysis

The Raman spectra of pristine PAniNT, GO, rGOA and PAniNT/rGOA are studied (**Figure 5.2**). The peaks at 1620 cm^{-1}, 1550 cm^{-1} and 1350 cm^{-1} are assigned to ν(C-C) vibration, imine ν(C=N) vibration band and semi-benzoid polaronic ν(C-N+•) of PAniNT respectively. The peak at 1200 cm^{-1} is indicative of the C-H in plane bending vibration of quinoid ring [27]. GO and rGOA exhibit two typical bands**.** The first band (*G band*) at 1608 cm^{-1} is ascribed to the graphitic structure and corresponds to the first order scattering of E_{2g} phonon of sp^2 carbon atoms at the Brillouin zone centre [28]. The second band (*D band*) at 1360-1385 cm^{-1} is due to the defects arising from structural edge effects, because of the breathing mode of k-point phonons with A_{1g} symmetry. The increase in the ratio of intensities of D and G bands (I_D/I_G) from 0.98 to 1.5 indicates reduction of GO to rGO during the aerogel formation process. This increase of ratio is due to the reduction of most of the functional groups containing oxygen as well as the decrease of average size of sp^2 domain. The spectrum of PAniNT/rGOA is almost similar with pristine PAniNT, however the peak intensity at 1620 cm^{-1} is slightly higher because of the presence of rGOA.

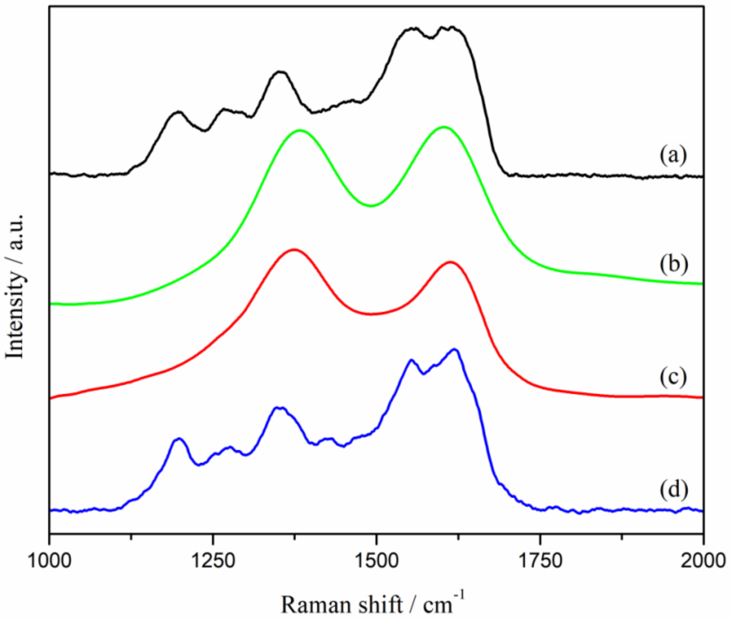

Figure 5.2. Raman spectra of **(a)** PAniNT, **(b)** GO, **(c)** rGOA and **(d)** PAniNT/rGOA.

5.3.1.3 XRD analysis

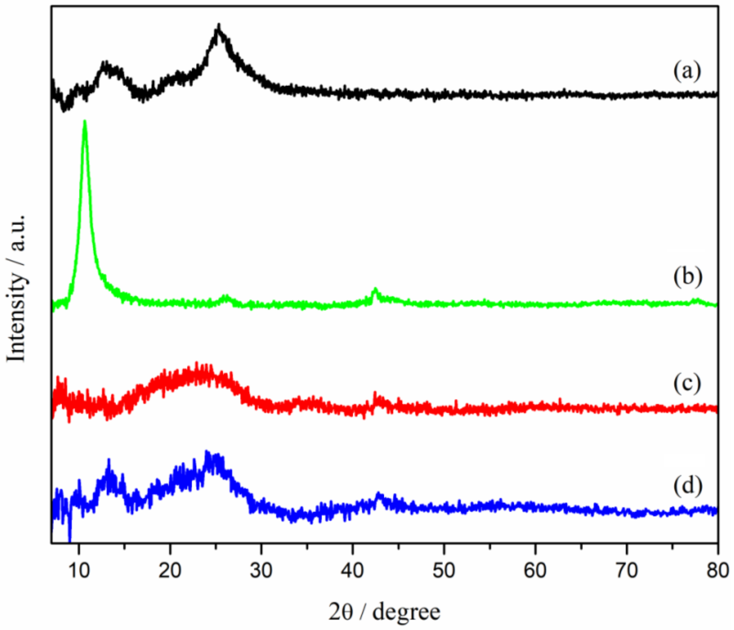

Figure 5.3. XRD patterns of **(a)** PAniNT, **(b)** GO, **(c)** rGOA and **(d)** PAniNT/rGOA.

Figure 5.3 exhibits the XRD peaks of PAniNT, GO, rGOA and PAniNT/rGOA. The XRD pattern of PAniNT is recognized by three typical broad peaks at 2θ = 14°, 20° and 25° due to the (011), (020) and (200) crystal planes of PAni. The broad nature of these peaks suggests partial crystallinity of the PAniNT [29,30]. The successful oxidation of graphite to GO via modified

Hummers method is shown by a sharp XRD peak at approximately 2θ = 10.6° due to the presence of (002) plane. The conversion of GO to rGOA is apparent in the XRD pattern of rGOA. A broad peak at around 2θ = 24° indicates the reduction of GO to rGOA [31]. The three broad peaks at 2θ = 13.3°, 21° and 25° are seen in the XRD plots of PAniNT/rGOA, which confirms the presence of PAniNT in the composite. The broadness of the peaks of PAniNT/rGOA also signifies the partial crystalline nature of the composite.

5.3.2 Morphological analysis

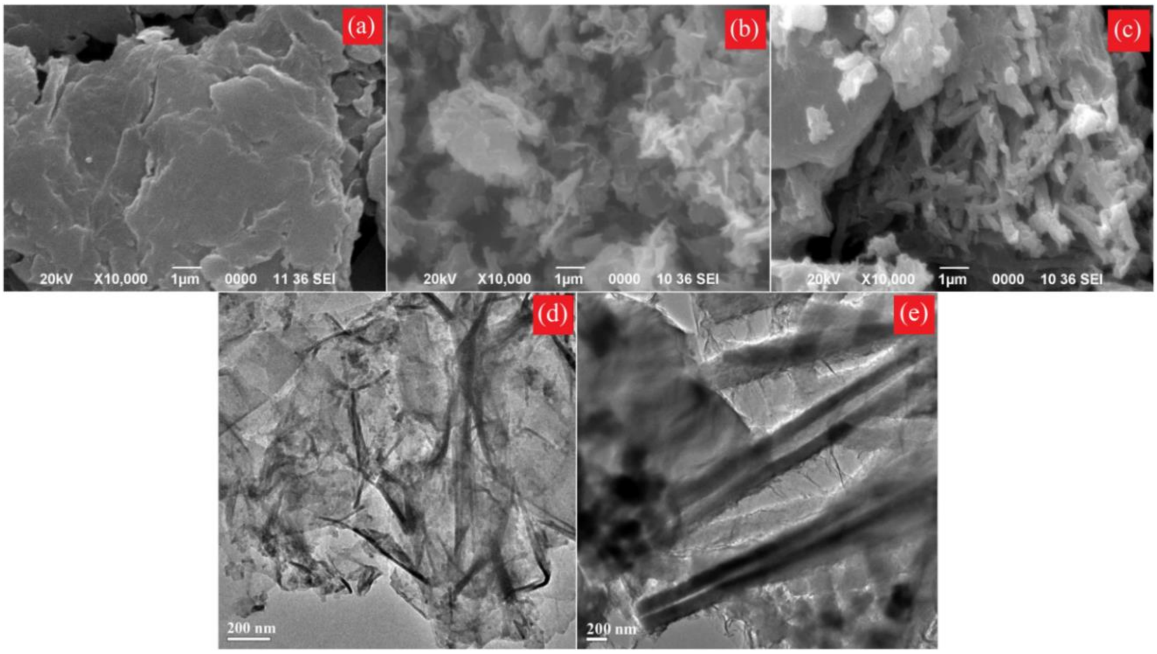

Figure 5.4. SEM micrographs of **(a)** GO, **(b)** rGOA and **(c)** PAniNT/rGOA, and TEM micrographs of **(d)** rGOA and **(e)** PAniNT/rGOA

Figure 5.4(a)-(c) show the SEM micrographs of the GO, rGOA and PAniNT/rGOA. Layers of sheets are observed in the micrograph of GO as shown in **Figure 5.4(a)**. The rGOA micrograph (**Figure 5.4(b)**) exhibits crumpled surfaces and sharp edges of graphene layers. In the **Figure 5.4(c),** PAniNTs are seen attached to the graphene sheets in the PAniNT/rGOA aerogel without any aggregation. **Figure 5.4(d)** displays the TEM micrograph of rGOA with a three dimensional inter-connected structure of small graphene layers. The nanotube structures of PAniNT on graphene sheets are observed in the TEM micrograph of PAniNT/rGOA **(Figure 5.4(e))**. The restacking of rGO sheets in PAniNT/rGOA is prevented to a large extent by the prominent π- π stacking between the hydrophobic basal planes of rGO and PAniNT in the aerogel. Furthermore, since GO is only partially reduced in the composite, hydrogen bonding between the hydrophilic oxygenated rGO and the aniline units of PAniNT may also occur.

5.3.3 Surface area determination

Brunauer-Emmett-Teller (BET) analysis was carried out to analyze the surface area of rGOA and PAniNT/rGOA. **Figure 5.5(a)** and **(b)** show the BET isotherms of rGOA and PAniNT/rGOA respectively. The hysteresis loop profile of both the aerogels is typical of Type-IV isotherm characteristic of mesoporous materials. The surface area based on BET model is found to be 168.39 m^2 g^{-1} and 294.73 m^2 g^{-1} for rGOA and PAniNT/rGOA respectively. The higher surface area of PAniNT/rGOA as compared to rGOA is due to the presence of PAniNT in the rGO aerogel matrix which prevents the restacking of rGO sheets to a significant extent.

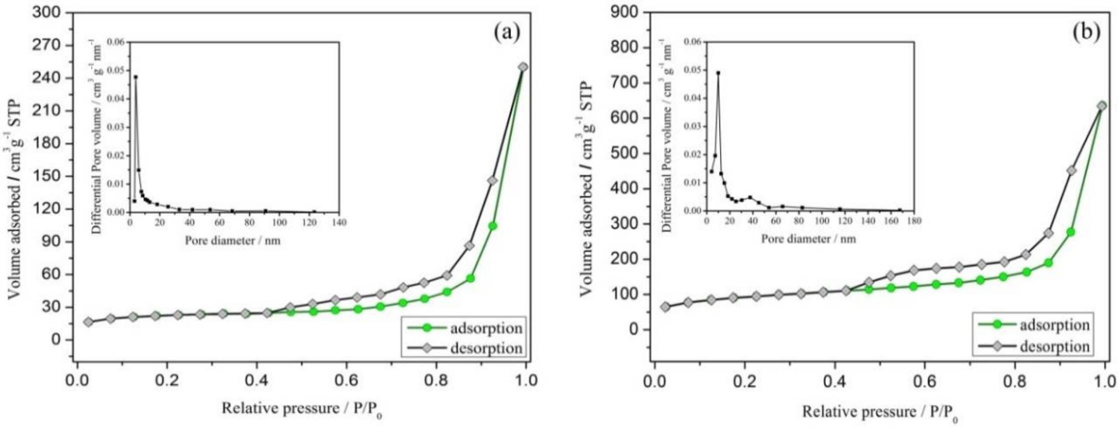

Figure 5.5. N_2 adsorption/desorption isotherms of **(a)** rGOA and **(b)** PAniNT/rGOA. The inset figures show corresponding pore size distribution of the aerogels (STP stands for standard temperature and pressure).

The pore volume is determined on the basis of Barrett–Joyner–Halenda (BJH) model. PAniNT/rGOA exhibits (1.94 cm^3 g^{-1}) slightly higher pore volume in comparison to rGOA (1.74 cm^3 g^{-1}). The insets of the **Figure 5.5(a)** and **(b)** exhibit the corresponding pore size distribution of the aerogels. Although rGOA shows a wide range of distribution of pore sizes from 3 to 124 nm, majority of them is concentrated between 3 to 20 nm with average pore size of 9.8 nm. Whereas PAniNT/rGOA exhibits slightly broader pore size distribution from 4 to 167 nm with average pore size of 10.1 nm. From the above study, one can conclude that the mesoporous structure with suitable pore sizes, high surface area and large pore volume of PAniNT/rGOA and rGOA are well suited as counter electrode materials of DSSC.

5.3.4 Electro-catalytic activity

Cyclic voltammograms were recorded to investigate the electrochemical behaviors of PAniNT, rGOA, PAniNT/rGOA and Pt electrodes. The characteristic CV plots for each electrode were recorded using an electrolyte contains 0.1 M lithium perchlorate ($LiClO_4$), 10 mM lithium iodide (LiI), and 1 mM iodine (I_2) in acetonitrile (scan rate is 50 mV s^{-1}) by applying a sweep potential from -0.5 V to 1.0 V. Ag/AgCl and a Pt wire are used as the reference and the counter electrode respectively. All the electrodes, except rGOA, exhibit two anodic and two cathodic current peaks (Ox-1/Red-1, Ox-2/Red-2, as labeled in **Figure 5.6**) analogous to **Eqs. (5.1)** and **(5.2)**.

$$I_3^- + 2e^- \leftrightarrow 3I^- \quad \ldots\ldots\ldots\ldots\ldots\ldots\ldots\ldots\ldots\ldots \quad \mathbf{(5.1)}$$

$$3I_2 + 2e^- \leftrightarrow 2I_3^- \quad \ldots\ldots\ldots\ldots\ldots\ldots\ldots\ldots\ldots\ldots \quad \mathbf{(5.2)}$$

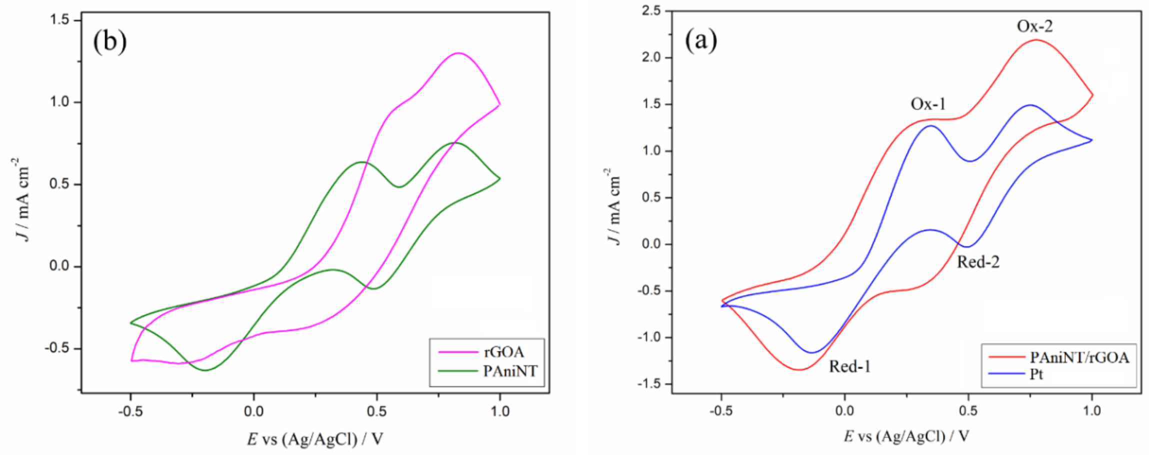

Figure 5.6. Cyclic voltammograms of **(a)** rGOA and PAniNT, and **(b)** PAniNT/rGOA and Pt electrodes in a three electrode set-up.

Our focus is on the characteristics peaks of the left redox pair (Ox-1 and Red-1) because they are responsible for reduction of triiodide ions (I_3^-) to iodide ions (I^-) at the counter electrode [32,33]. The catalytic activity of the counter electrode is quantitatively described by the peak current (I_P) and peak-to-peak separation voltage (E_{PP}) of Ox-1 and Red-1 process. Better electro-catalytic behavior of the counter electrode is indicated by higher I_P and lower E_{PP} values. Additionally, the electrical conductivity of the counter electrode materials is directly correlated to their peak currents. The anodic peak current density (I_{Pa}), cathodic peak current density (I_{Pc}) and E_{PP} values of different electrodes are tabulated in **Table 5.1.** The rGOA electrode shows the lowest magnitude of I_{Pc} of -0.59 mA cm^{-2} amongst all the electrodes because of its lower catalytic behavior towards the reduction of I_3^- ions. The PAniNT/rGOA electrode exhibits slightly higher I_{Pc} (-1.34 mA cm^{-2}) and I_{Pa} (1.35 mA cm^{-2}) values than the Pt counter electrode (I_{Pc} is -1.16 mA cm^{-2} and I_{Pa} is 1.27 mA cm^{-2}). This is due to the large active surface area conferred by the prepared aerogel. Another interesting parameter that can be obtained from the CV curve is E_{PP}, which can be related inversely to the electrochemical reversibility of the system. The E_{PP} value for PAniNT/rGOA is 0.50 V, which is comparable with that of Pt (0.47

V). This study proves that the incorporation of catalytically active PAniNT in conductive rGOA with high surface area can efficiently enhance the reduction kinetics of I_3^- ions. Additionally, the area inside the curve also increases in case of the PAniNT/rGOA electrode. This is due to the electrochemical double layer capacitive behavior shown by high surface area of graphene based aerogel.

Figure 5.7(a) shows the cyclic voltammograms of PAniNT/rGOA electrode at various scan rates. The current densities increase with the increment of scan rate. Also, the anodic peak and the corresponding cathodic peak gradually shifts towards positive and negative directions respectively.

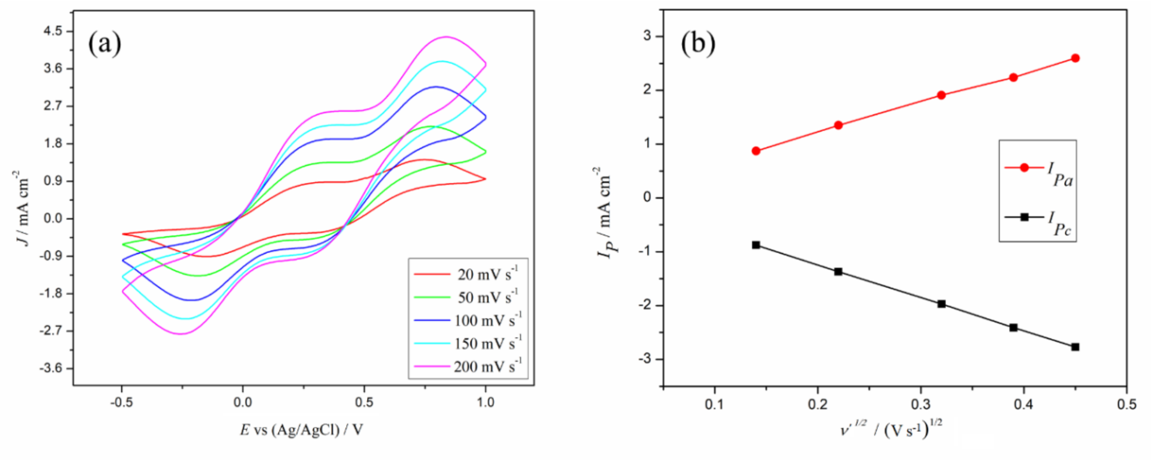

Figure 5.7. (a) Cyclic voltammograms of PAniNT/rGOA electrode at different scan rates (from inner to outer: 20, 50, 100, 150 and 200 mV s^{-1}) and **(b)** the relationship between peak current densities and the square root of the scan rate for Ox-1/Red-1.

Figure 5.7(b) exhibits the relationship of peak current densities of Ox-1/Red-1 with the square root of scan rate. The linear relationship tells that the ionic diffusion of redox species in the electrolyte controls the redox reactions on the PAniNT/rGOA electrode and obeys Randles-Sevcik equation (**Eq. (5.3)**) [34].

$$I_p = K'n^{3/2}AD^{1/2}C_o^{*}v'^{1/2} \;\ldots\ldots\ldots\ldots\ldots\ldots\ldots\ldots\ldots\ldots\ldots\ldots\ldots \;\mathbf{(5.3)}$$

where *K'* is a constant (2.69×10^5), *n* = 2 is the number of electrons involving in the charge transfer process, *A* is the area of the electrode, *D* is the diffusion coefficient of I_3^- ions, *C** is the bulk concentration of I_3^- species and *v'* is the applied scan rate. The calculated diffusion coefficients of I_3^- ions at different counter electrodes are listed in **Table 5.1**. The PAniNT/rGOA electrode exhibits slightly better diffusion coefficient (2.481×10^{-5} cm^2 s^{-1}) of I_3^- ions than the Pt electrode (1.859×10^{-5} cm^2 s^{-1}) indicating good catalytic performances of the aerogel electrode.

This is due to the higher active surface area present in the mesoporous structure of PAniNT/rGOA.

Table 5.1. Electrochemical parameters of different electrodes derived from CV measurements.

Electrode	I_{Pc} / mA cm^{-2}	I_{Pa} / mA cm^{-2}	E_{PP} / V	D / cm^2 s^{-1}
Pt	-1.16	1.27	0.47	1.859×10^{-5}
rGOA	-0.59	0.98	0.86	0.481×10^{-5}
PAniNT	-0.64	0.64	0.62	0.566×10^{-5}
PAniNT/rGOA	-1.34	1.35	0.50	2.481×10^{-5}

The stability of the PAniNT/rGOA counter electrode is demonstrated in 100 conjugative cyclic voltammograms, recorded by applying a scan rate of 50 mV s^{-1} (**Figure 5.8**). The voltammograms exhibit well repetition of peak current positions showing good stability of the counter electrode material.

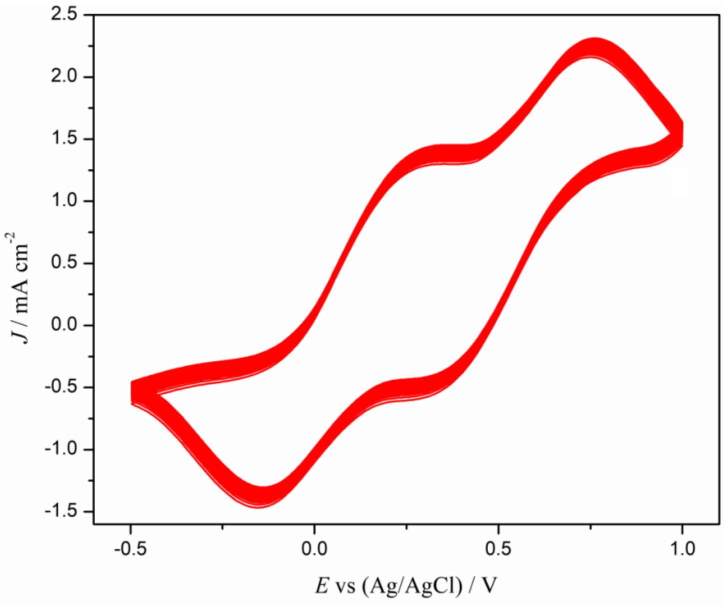

Figure 5.8. Cyclic voltammograms of PAniNT/rGOA electrode for 100 cycles.

5.3.5 Tafel plots

Tafel analysis was carried out to understand the electrochemical kinetic processes occuring at different electrodes. Tafel plots were recorded by applying a potential sweep on the symmetrical dummy cells prepared by sandwiching the PGE in between two similar electrodes. **Figure 5.9** illustrates the Tafel curves of PAniNT, rGOA, PAniNT/rGOA and Pt electrodes. The Tafel polarization curve is typically divided into three parts: the high potential region, the middle range

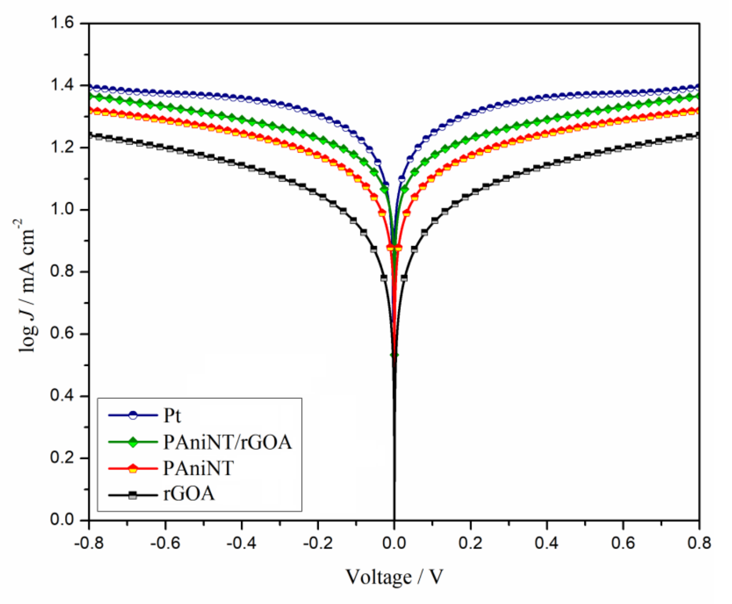

Figure 5.9. Tafel plots of Pt, PAniNT/rGOA, PAniNT and rGOA electrodes for the symmetrical dummy cells.

Table 5.2. J_0 and J_{lim} data for the symmetrical dummy cells of different types of electrodes.

Electrode	J_0 / mA cm^{-2}	J_{lim} / mA cm^{-2}
Pt	13.72	24.55
rGOA	7.67	16.98
PAniNT	10.84	20.42
PAniNT/rGOA	12.21	22.91

and the low potential region, and they represent the diffusion region, Tafel region and polarization region respectively [35]. The exchange current density (J_0) can be calculated from the polarization region, while the limiting current density (J_{lim}) can be measured from the diffusion region. The magnitude of J_0 represents the rate of the reduction of I_3^- ions at the catalytically active surface of counter electrode. Thus J_0 is directly correlated with the number of active catalytic sites present in the counter electrode. J_0 and J_{lim} values obtained from the Tafel plots are summarized in **Table 5.2**. The low J_0 value (10.84 mA cm^{-2}) of PAniNT indicates lower conductivity and electro-catalytic activity in comparison to Pt electrode (13.72 mA cm^{-2}). However, incorporation of PAniNT in mesoporous rGOA increases the J_0 value to 12.21 mA cm^{-2} indicating enhancement of the reduction rate of I_3^- ions at the electrode. It is conclusive from this study that PAniNT/rGOA electrode can reduce I_3^- ions, comparable to that of Pt electrode.

5.3.6 Photovoltaic performance

The *J-V* characteristics of the fabricated DSSCs employing different counter electrodes are studied under irradiation of 100 mW cm^{-2} light **(Figure 5.10(a))**. The detailed photovoltaic parameters are listed in **Table 5.3**. The DSSC fabricated with rGOA counter electrode shows the lowest efficiency of 3.29% with open-circuit voltage (V_{OC}) of 0.755 V, short-circuit current density (J_{SC}) of 7.59 mA cm^{-2} and fill factor (*FF*) of 0.57. The DSSC with PAniNT counter electrode exhibits slightly higher efficiency of 4.13% with V_{OC} of 0.775 V, J_{SC} of 9.09 mA cm^{-2} and *FF* of 0.58 due to the higher catalytic activity. When PAniNT is added to the rGOA matrix, it causes an improvement in the photovoltaic parameters of the DSSC. DSSCs with counter electrodes having different content of PAniNT are also studied to observe their effect **(Figure 5.10(b))**. PAniNT/rGOA, PAniNT/rGOA(0.8), PAniNT/rGOA(1.2) and PAniNT/rGOA(0.6)

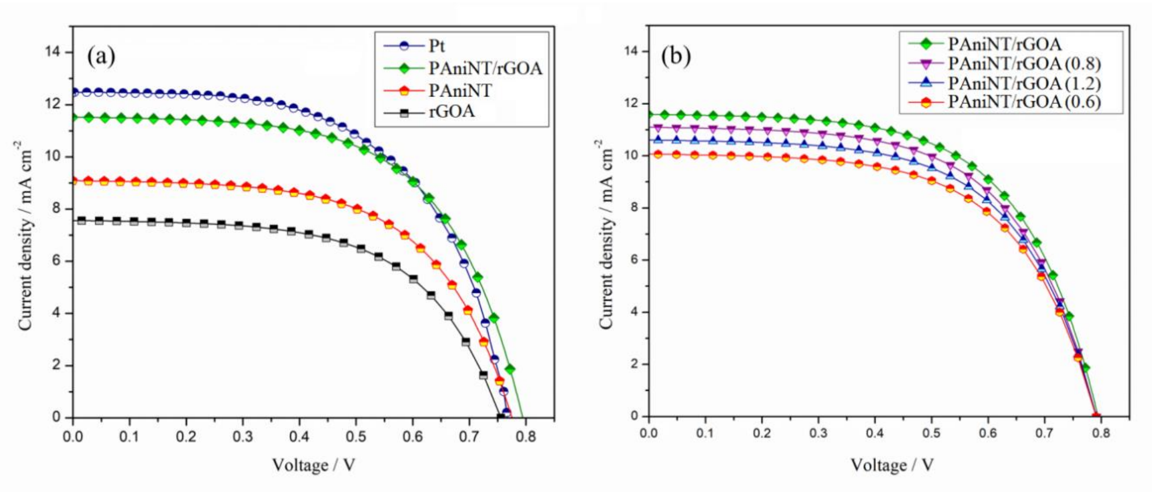

Figure 5.10. *J-V* characteristics of DSSCs fabricated with **(a)** rGOA, PAniNT, PAniNT/rGOA and Pt counter electrodes, and **(b)** electrodes with different PAniNT content in rGOA.

represent aerogels with PAniNT:rGO ratio of 1:1, 0.8:1, 1.2:1 and 0.6:1 respectively. A trend of improvement in the photoelectric performances with increasing PAniNT content in rGOA is observed. The optimum result is obtained when the ratio of PAniNT to rGO aerogel is 1:1. The DSSC fabricated with PAniNT/rGOA counter electrode shows efficiency of 5.47% with V_{OC}, J_{SC} and *FF* values of 0.794 V, 11.50 mA cm^{-2} and 0.59 respectively. The maximum efficiency shown by PAniNT/rGOA counter electrode is at par with the Pt counter electrode (efficiency 5.54%), asserting its capability to replace the costly Pt counter electrode in DSSCs.

Table 5.3. Photovoltaic parameters for the DSSCs employing different counter electrodes.

Electrode	V_{OC} / V	J_{SC} / mA cm^{-2}	***FF***	η / %
Pt	0.766	12.49	0.57	5.54
rGOA	0.755	7.56	0.57	3.29
PAniNT	0.775	9.09	0.58	4.13
PAniNT/rGOA(0.6)	0.790	10.14	0.59	4.75
PAniNT/rGOA(0.8)	0.791	11.10	0.59	5.20
PAniNT/rGOA	0.794	11.50	0.59	5.47
PAniNT/rGOA(1.2)	0.791	10.77	0.59	5.02

In order to see the effect of thickness of the counter electrode film, the photovoltaic parameters of the DSSCs are studied by varying its thickness from 1.87 µm to 10.32 µm. As PAniNT/rGOA exhibits the maximum photoconversion efficiency among all the prepared composite aerogels, it is chosen as the test material (**Figure 5.11(a)** and **(b)**). Both J_{SC} and V_{OC} values rise gradually with growing thickness upto 9-10 µm. The thinner counter electrode layers have lesser number of catalytic sites resulting in less electron transfer process at the counter electrode/electrolyte interface. However, when the layers become thick, the rate of reduction of I_3^- ions increases because of the availability of larger number of catalytic active sites as well as an augmented surface area. Hence, an improvement is observed in the photovoltaic parameters of DSSC including *FF* and efficiency. The *FF* obtained in our devices is more than 0.50, which is the typical value for *FF* of conventional photovoltaic cells. It is an indication that recombination process, which is a major contributor to loss of current in semiconductor based devices, has been minimized [36]. However beyond 10 μm, increase in the film thickness has negligible impact on the device performance. This is due to the enhancement of the charge and mass transport resistances with the increment of the film thickness.

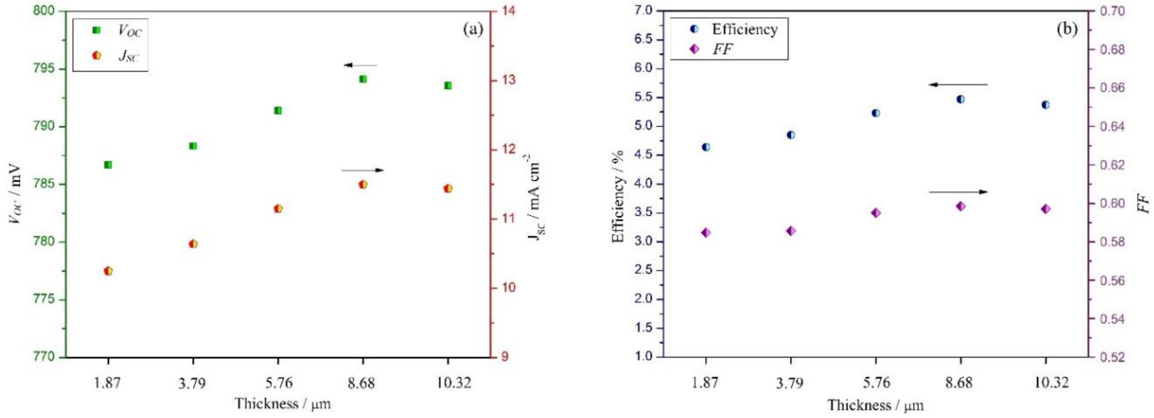

Figure 5.11. Photovoltaic parameters of DSSCs fabricated with PAniNT/rGOA counter electrodes of different thicknesses.

5.3.7 Contribution of gel electrolyte to the performance of DSSC

The use of PGE in DSSCs is very advantageous as it prevents leakage and evaporation of the solvent. In addition, it contributes to the performance of the DSSC in many other ways as described in the following section.

5.3.7.1 Enhancement in V_{OC}

To study the role of PGE, *J-V* characteristics of DSSCs employing liquid electrolyte under illumination of 100 mW cm^{-2} light was recorded and compared with the DSSC employing PGE. (**Figure 5.12(a)**). PAniNT/rGOA counter electrode was used to fabricate both the DSSCs. The DSSC fabricated with liquid electrolyte exhibits efficiency of 5.89% with V_{OC}, J_{SC} and *FF* values of 0.738 V, 12.69 mA cm^{-2} and 0.62 respectively. The DSSC employing PGE shows efficiency of 5.47% with V_{OC}, J_{SC} and *FF* values of 0.794 V, 11.50 mA cm^{-2} and 0.59 respectively. An enhancement in V_{OC} from 0.738 V to 0.794 V is observed for the PGE. This enhancement is crucial for the performance of the DSSC fabricated with PGE. To understand it, the chemical capacitance of the DSSCs at the photoanode/electrolyte interface is studied using EIS under dark conditions at different bias. **Figure 5.12(b)** shows the effect of applied bias on $C\mu$ values in both liquid electrolyte and PGE. V_{OC} is defined as the difference between the potential of the quasi Fermi level of TiO_2 (E_F) and the redox potential (E_{redox}) of the redox couple. E_F can be expressed in terms of conduction band edge of TiO_2 (E_C). The overall expression correlating V_{OC} with E_C and E_{redox} is expressed in **Eq. (5.4)**.

$$V_{oc}=\frac{kT}{q}\left(\frac{E_C-E_{redox}}{kT}+\ln\frac{n_c}{N_C}\right)\ldots\ldots\ldots\ldots\ldots\ldots\ldots\ldots\ldots\ldots\ldots\ldots\ldots\ldots\ldots\ldots \mathbf{(5.4)}$$

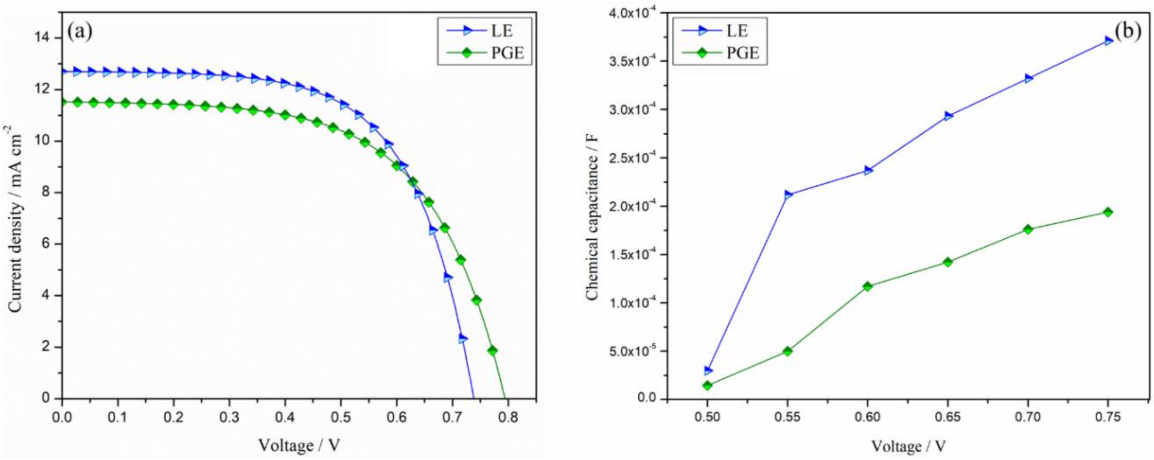

Figure 5.12. Comparison between performances of DSSCs fabricated with PAniNT/rGOA counter electrode employing liquid electrolyte (LE) and PGE in terms of **(a)** J-V characteristics and **(b)** chemical capacitances at the photoanode/electrolyte interface at various applied potentials.

where k, T, $n_{c,}$ N_C and q are Boltzmann constant, temperature, free electron density at conduction band of TiO_2, density of accessible state in the conduction band of TiO_2 and charge respectively. E_C can be quantitatively estimated from the value of $C\mu$, which is determined from the accumulated electron density at the TiO_2/electrolyte interface [37–39]. It can be seen from **Figure 5.12(b)** that at a given bias potential, the capacitance of PGE is lower than that of the liquid electrolyte. The double layer capacitance at the photoanode/gel electrolyte is decreased due to the restricted movement of Li^+ ions in polymer matrix. The electron rich groups present in the PMMA interacts with the positively charged Li^+ ions inhibiting the movement of Li^+ ions. As a result, a negative shift of V_{OC} takes place resulting in enhancement of V_{OC} of the device [37].

5.3.7.2 Long-term stability

Another striking difference between the liquid electrolyte and the PGE is its long-term stability. **Figure 5.13(a)** and **(b)** exhibit the variation of J_{SC} and V_{OC} values of DSSCs fabricated with PAniNT/rGOA counter electrode employing PGE and liquid electrolyte for duration of 1000 h in air at room temperature. DSSC employing liquid electrolyte shows a sharp decay of J_{SC}

value after 200 h of testing due to the leakage and volatilization of the solvent. However, DSSC fabricated with PGE retains 92% of initial current indicating better long-term stability. On the other hand, V_{OC} values with both the liquid electrolyte and the PGE remain mostly unaffected. In conclusion of this study, the DSSC with the PGE encumbers the leakage and volatilization of solvents to provide better long-term stability.

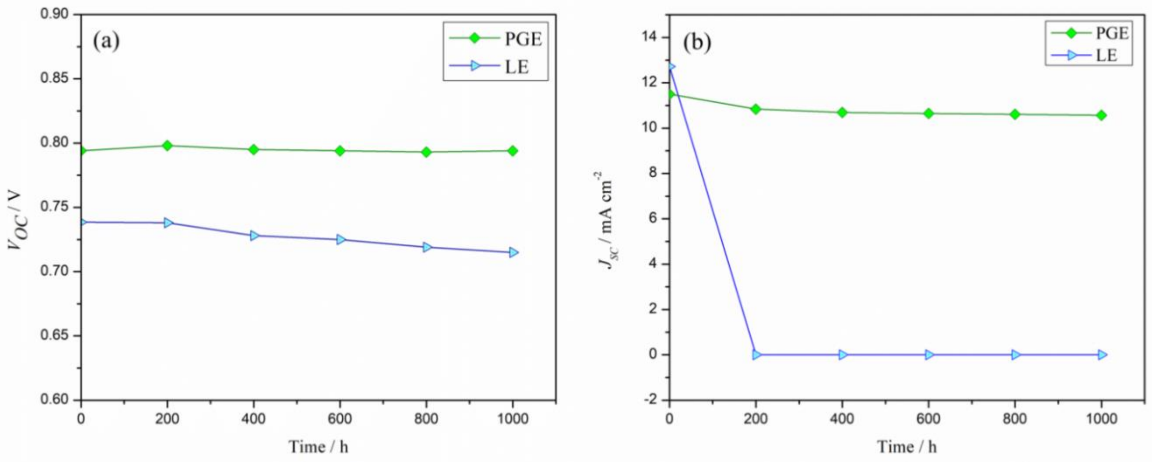

Figure 5.13. Long-term stability of DSSCs over a period of 1000 h in terms of **(a)** V_{OC} and **(b)** J_{SC} values.

5.3.8. Electrochemical impedance spectroscopy study

To obtain further insight into the interfacial charge transfer processes of the fabricated devices, EIS data was recorded under illumination. On the basis of transmission line model, the EIS data can be fitted with an equivalent circuit giving rise to the Nyquist plot. The Z' vs $-Z''$ plot displays three semicircles **(Figure 5.14)** [40,41]. The semicircle in the high frequency region represents the charge transfer at the counter electrode/electrolyte interface ($R_{CT,CE}$), the middle range is assigned to the charge transfer at the TiO_2/electrolyte interface (R_{CT}) and the low frequency region is related to the ionic diffusion in the electrolyte. The intercept point on the real axis represents the internal series resistance (R_S). The data of R_S, R_{CT} and $R_{CT,CE}$ for different DSSCs employing the PGE are tabulated in **Table 5.4.** The composite aerogel, PAniNT/rGOA shows 1.13 Ω resistance ($R_{CT,CE}$) at the counter electrode/electrolyte interface which is lower in comparison to those of rGOA (1.87 Ω) and PAniNT (1.30 Ω) electrodes. The lower value of $R_{CT,CE}$ of PAniNT/rGOA infers higher charge transfer kinetics at the electrode/electrolyte interface. Thus, faster rate of reduction of I_3^- ions occurs at the PAniNT/rGOA electrode in comparison to those of PAniNT and rGOA electrodes. This is due to the presence of a larger surface area, suitable pore size distribution and abundance of catalytically active sites on the mesoporous PAniNT/rGOA. Additionally, the charge transfer kinetics at the PAniNT/rGOA electrode is quite comparable with that of the Pt electrode ($R_{CT,CE}$ of Pt = 1.02 Ω) as the $R_{CT,CE}$ values of both the materials are almost similar.

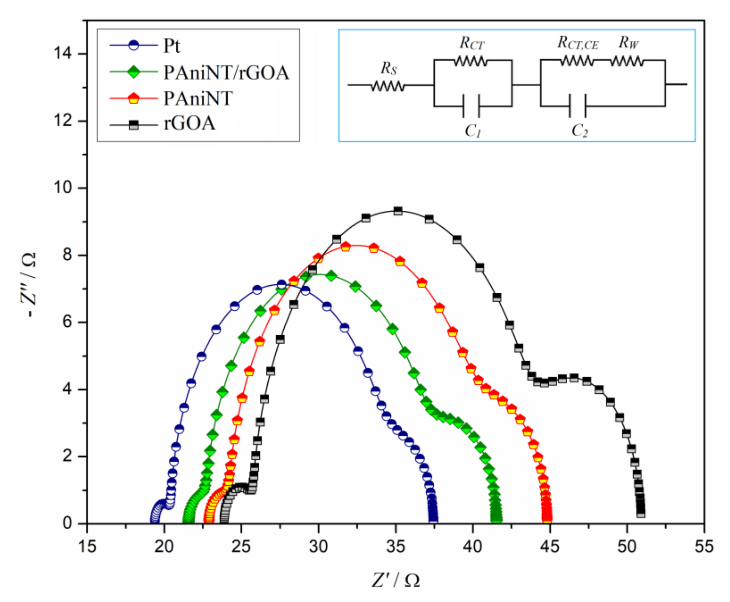

Figure 5.14. Nyquist plots of EIS data of the DSSCs fabricated using Pt, PAniNT/rGOA, PAniNT and rGOA counter electrodes under irradiation of light. The inset shows the corresponding equivalent circuit model.

Table 5.4. R_S, $R_{CT,CE}$ and R_{CT} data for the DSSCs fabricated with different counter electrodes.

Electrode	R_S / Ω	$R_{CT,CE}$ / Ω	R_{CT} / Ω
Pt	19.38	1.02	13.84
rGOA	23.87	1.87	18.05
PAniNT	22.89	1.30	15.87
PAniNT/rGOA	21.57	1.13	14.36

Furthermore, EIS is used to calculate the values of chemical capacitance ($C\mu_{,CE}$) at the counter electrode/electrolyte interface by concentrating on the semicircle in the higher frequency region. The values of $C\mu_{,CE}$ are studied to examine the behavior of the surface of counter electrodes. The $C\mu_{,CE}$ values are tabulated in **Table 5.5**. The surface area of the counter electrode plays a crucial role in the determination of $C\mu_{,CE}$, which in turn reflects in the value of V_{OC}. Higher value of $C\mu_{,CE}$ implies better value of V_{OC}. Among all the counter electrodes, PAniNT/rGOA exhibits significantly higher value of 41.7 μF because of higher surface area as compared to other electrodes. Thus, the highly porous aerogel structure of PAniNT/rGOA enhances the V_{OC} values, which in turn, improves the efficiency of the fabricated device.

Table 5.5. Chemical capacitance at the counter electrode/electrolyte interface of symmetrical dummy cells with 0.75 V applied bias.

Electrode	Pt	rGOA	PAniNT	PAniNT/rGOA
$C\mu_{,CE}$ / μF	22.62	32.65	20.41	41.7

5.4 Conclusion

- A graphene based PAniNT/rGOA counter electrode material was successfully synthesized for fabricating quasi-solid-state DSSCs by incorporating PAniNT in rGOA in different mass ratios.
- Morphology analysis and surface area determination were carried out. The PAniNT/rGOA composite with mass ratio 1:1 exhibited a surface area of 294.73 m^2 g^{-1} with average pore size of 10.1 nm.
- Cyclic voltammogram of PAniNT/rGOA revealed its high catalytic activity towards the reduction of the triiodide ions. Furthermore, cyclic voltammograms with 100 cycles showed significant stability of the material in the cell environment.
- The exchange current density computed from the Tafel plot of PAniNT/rGOA was found to be 12.21 mA cm^{-2}, which was quite comparable to the value observed in Pt counter electrode (13.72 mA cm^{-2}).
- A photoconversion efficiency of 5.47% with V_{OC} value of 0.794 V, J_{SC} value of 11.50 mA cm^{-2} and *FF* value of 0.59 was achieved from the optimized DSSC fabricated with PAniNT/rGOA counter electrode employing PGE (PMMA based electrolyte with 0.57 wt% CB) under irradiation of 100 mW cm^{-2} (AM 1.5) light.
- The DSSC exhibited a significant enhancement of V_{OC} from 0.738 V to 0.794 V because of the restricted movement of Li^+ ions in the polymer matrix. The non-faradic process (double layer capacitance) at the large surface area of PAniNT/rGOA also contributed to the enhancement of V_{OC}.
- The same DSSC showed significant durability by retaining 92% of its initial value of J_{SC}.

These studies alluded to the feasibility of PAniNT/rGOA counter electrode as an efficient, low-cost alternative to the costly Pt counter electrode.

5.5 References

[1] Wang, G., Xing, W., and Zhuo, S. The production of polyaniline/graphene hybrids for use as a counter electrode in dye-sensitized solar cells. *Electrochimica Acta*, 66:151-157, 2012.

[2] Li, Q., Wu, J., Tang, Q., Lan, Z., Li, P., Lin, J., and Fan, L. Application of microporous polyaniline counter electrode for dye-sensitized solar cells. *Electrochemistry Communications*, 10(9):1299-1302, 2008.

[3] Wang, H., Feng, Q., Gong, F., Li, Y., Zhou, G., and Wang, Z. S. In situ growth of oriented polyaniline nanowires array for efficient cathode of Co(iii)/Co(ii) mediated dye-sensitized solar cell. *Journal of Materials Chemistry A*, 1(1):97-104, 2013.

[4] Xiao, Y. M., Lin, J. Y., Wu, J. H., Tai, S. Y., and Yue, G. T. Pulse potentiostatic electropolymerization of high performance PEDOT counter electrodes for Pt-free dye-sensitized solar cells. *Electrochimica Acta*, 83:221-226, 2012.

[5] Trevisan, R., Döbbelin, M., Boix, P. P., Barea, E. M., Tena-Zaera, R., Mora-Seró, I., and Bisquert, J. PEDOT nanotube arrays as high performing counter electrodes for dye sensitized solar cells. Study of the interactions among electrolytes and counter electrodes. *Advanced Energy Materials*, 1(5):781-784, 2011.

[6] Jeon, S. S., Kim, C., Ko, J., and Im, S. S. Spherical polypyrrole nanoparticles as a highly efficient counter electrode for dye-sensitized solar cells. *Journal of Materials Chemistry*, 21(22):8146-8151, 2011.

[7] Bu, C., Tai, Q., Liu, Y., Guo, S., and Zhao, X. A transparent and stable polypyrrole counter electrode for dye-sensitized solar cell. *Journal of Power Sources*, 221:78-83, 2013.

[8] Han, J., Kim, H., Kim, D. Y., Jo, S. M., and Jang, S. Y. Water-soluble polyelectrolyte-grafted multiwalled carbon nanotube thin films for efficient counter electrode of dye-sensitized solar cells. *ACS Nano*, 4(6):3503-3509, 2010.

[9] Benedetti, J. E., Corrêa, A. A., Carmello, M., Almeida, L. C., Gonçalves, A. S., and Nogueira, A. F. Cross-linked gel polymer electrolyte containing multi-wall carbon nanotubes for application in dye-sensitized solar cells. *Journal of Power Sources*, 208:263-270, 2012.

[10] Brown, P., Takechi, K., and Kamat, P. V. Single-walled carbon nanotube scaffolds for dye-sensitized solar cells. *Journal of Physical Chemistry C*, 112(12):4776-4782, 2008.

[11] Zhang, D. W., Li, X. D., Li, H. B., Chen, S., Sun, Z., Yin, X.J., and Huang, S. M. Graphene-based counter electrode for dye-sensitized solar cells. *Carbon*, 49(15):5382-5388, 2011.

[12] Li, G. R., Wang, F., Song, J., Xiong, F. Y., and Gao, X. P. TiN-conductive carbon black composite as counter electrode for dye-sensitized solar cells. *Electrochimica Acta*, 65:216-220, 2012.

[13] Brennan, L. J., Byrne, M. T., Bari, M., and Gun'ko, Y. K. Carbon nanomaterials for dye-sensitized solar cell applications: A bright future. *Advanced Energy Materials*, 1(4):472-485, 2011.

[14] Li, G. R., Wang, F., Jiang, Q. W., Gao, X. P., and Shen, P. W. Carbon nanotubes with titanium nitride as a low-cost counterelectrode material for dye-sensitized solar cells. *Angewandte Chemie - International Edition*, 49(21):3653-3656, 2010.

[15] Cheng, W. Y., Wang, C. C., and Lu, S. Y. Graphene aerogels as a highly efficient counter electrode material for dye-sensitized solar cells. *Carbon*, 54:291-299, 2013.

[16] Xu, Y., Bai, H., Lu, G., Li, C., and Shi, G. Flexible graphene films via the filtration of water-soluble noncovalent functionalized graphene sheets. *Journal of the American Chemical Society*, 130(18):5856-5857, 2008.

[17] Xue, Y., Liu, J., Chen, H., Wang, R., Li, D., Qu, J., and Dai, L. Nitrogen-doped graphene foams as metal-free counter electrodes in high-performance dye-sensitized solar cells. *Angewandte Chemie - International Edition*, 51(48):12124-12127, 2012.

[18] Yang, Y., Zhao, B., Tang, P., Cao, Z., Huang, M., and Tan, S. Flexible counter electrodes based on nitrogen-doped carbon aerogels with tunable pore structure for high-performance dye-sensitized solar cells. *Carbon*, 77:113-121, 2014.

[19] Paulchamy, B., Arthi, G., and Lignesh, B. D. A simple approach to stepwise synthesis of graphene oxide nanomaterial. *Journal of Nanomedicine & Nanotechnology*, 6(1):1, 2015.

[20] Huang, Z., Liu, E., Shen, H., Xiang, X., Tian, Y., Xiao, C., and Mao, Z. Preparation of polyaniline nanotubes by a template-free self-assembly method. *Materials Letters*, 65(13):2015-2018, 2011.

[21] Mohan, K., Dolui, S., Nath, B. C., Bora, A., Sharma, S., and Dolui, S. K. A highly stable and efficient quasi solid state dye sensitized solar cell based on polymethyl methacrylate (PMMA)/carbon black (CB) polymer gel electrolyte with improved open circuit voltage. *Electrochimica Acta*, 247:216-228, 2017.

[22] Li, Q., Wu, J., Tang, Z., Xiao, Y., Huang, M., and Lin, J. Application of poly(acrylic acid-g-gelatin)/polypyrrole gel electrolyte in flexible quasi-solid-state dye-sensitized solar cell. *Electrochimica Acta*, 55(8):2777-2781, 2010.

[23] Lin, L. Y., Tsai, C. H., Wong, K. T., Huang, T. W., Hsieh, L., Liu, S. H., Lin, H. W., Wu, C. C., Chou, S. H., Chen, S. H., and Tsai, A. I. Organic dyes containing coplanar diphenyl-substituted dithienosilole core for efficient dye-sensitized solar cells. *Journal of*

Organic Chemistry, 75(14):4778-4785, 2010.

[24] Yu, J., Fan, J., and Lv, K. Anatase TiO_2 nanosheets with exposed (001) facets: Improved photoelectric conversion efficiency in dye-sensitized solar cells. *Nanoscale*, 2(10):2144-2149, 2010.

[25] Xu, F., Zheng, G., Wu, D., Liang, Y., Li, Z., and Fu, R. Improving electrochemical performance of polyaniline by introducing carbon aerogel as filler. *Physical Chemistry Chemical Physics*, 12(13):3270-3275, 2010.

[26] Huang, X., Hu, N., Gao, R., Yu, Y., Wang, Y., Yang, Z., Kong, E. S. W., Wei, H., and Zhang, Y. Reduced graphene oxide-polyaniline hybrid: Preparation, characterization and its applications for ammonia gas sensing. *Journal of Materials Chemistry*, 22(42):22488-22495, 2012.

[27] Wang, H., Hao, Q., Yang, X., Lu, L., and Wang, X. A nanostructured graphene/polyaniline hybrid material for supercapacitors. *Nanoscale*, 2(10):2164-2170, 2010.

[28] Xu, C., Shi, X., Ji, A., Shi, L., Zhou, C., and Cui, Y. Fabrication and characteristics of reduced graphene oxide produced with different green reductants. *PLoS ONE*, 10(12):e0144842, 2015.

[29] Jin, L., Jiang, Y., Zhang, M., Li, H., Xiao, L., Li, M., and Ao, Y. Oriented polyaniline nanowire arrays grown on dendrimer (PAMAM) functionalized multiwalled carbon nanotubes as supercapacitor electrode materials. *Scientific Reports*, 8(1):6268, 2018.

[30] Khalid, M., Acuna, J. J., Tumelero, M. A., Fischer, J. A., Zoldan, V. C., and Pasa, A. A. Sulfonated porphyrin doped polyaniline nanotubes and nanofibers: Synthesis and characterization. *Journal of Materials Chemistry*, 22(22):11340-11346, 2012.

[31] Mishra, S. K., Tripathi, S. N., Choudhary, V., and Gupta, B. D. SPR based fibre optic ammonia gas sensor utilizing nanocomposite film of PMMA/reduced graphene oxide prepared by in situ polymerization. *Sensors and Actuators B-Chemical*, 199:190-200, 2014.

[32] Gong, F., Xu, X., Zhou, G., and Wang, Z. S. Enhanced charge transportation in a polypyrrole counter electrode via incorporation of reduced graphene oxide sheets for dye-sensitized solar cells. *Physical Chemistry Chemical Physics*, 15(2):546-552, 2013.

[33] Sun, W., Peng, T., Liu, Y., Xu, S., Yuan, J., Guo, S., and Zhao, X. Z. Hierarchically porous hybrids of polyaniline nanoparticles anchored on reduced graphene oxide sheets as counter electrodes for dye-sensitized solar cells. *Journal of Materials Chemistry A*, 1(8):2762-2768, 2013.

[34] Bard, A. J. and Faulkner, L. R. *Electrochemical methods : Fundamentals and*

applications. Wiley, New York, 2nd edition, 2001.

[35] Yue, G., Ma, X., Zhang, W., Li, F., Wu, J., and Li, G. A highly efficient flexible dye-sensitized solar cell based on nickel sulfide/platinum/titanium counter electrode. *Nanoscale Research Letters*, 10(1):1-9, 2015.

[36] O'Regan, B. and Grätzel, M. A low-cost, high-efficiency solar cell based on dye-sensitized colloidal TiO_2 films. *Nature*, 353(6346):737-740, 1991.

[37] Wu, C., Jia, L., Guo, S., Han, S., Chi, B., Pu, J., and Jian, L. Open-circuit voltage enhancement on the basis of polymer gel electrolyte for a highly stable dye-sensitized solar cell. *ACS Applied Materials and Interfaces*, 5(16):7886-7892, 2013.

[38] Barea, E. M., Ortiz, J., Payá, F. J., Fernández-Lázaro, F., Fabregat-Santiago, F., Sastre-Santos, A., and Bisquert, J. Energetic factors governing injection, regeneration and recombination in dye solar cells with phthalocyanine sensitizers. *Energy and Environmental Science*, 3(12):1985-1994, 2010.

[39] Bisquert, J. Chemical capacitance of nanostructured semiconductors: Its origin and significance for nanocomposite solar cells. *Physical Chemistry Chemical Physics*, 5(24):5360-5364, 2003.

[40] Bisquert, J. Theory of the impedance of electron diffusion and recombination in a thin layer. *Journal of Physical Chemistry B*, 106(2):325-333, 2002.

[41] Bisquert, J., Grätzel, M., Wang, Q., and Fabregat-Santiago, F. Three-channel transmission line impedance model for mesoscopic oxide electrodes functionalized with a conductive coating. *Journal of Physical Chemistry B*, 110(23):11284-11290, 2006.